Research Paper

# Synergistic effect of oxygen species and vacancy for enhanced electrochemical $CO_2$ conversion to formate on indium oxide

Tengfei Ma [1], Zihao Jiao [1], Haoran Qiu [1], Feng Wang, Ya Liu [*], Liejin Guo [*]

*International Research Center for Renewable Energy, State Key Laboratory of Multiphase Flow in Power Engineering, Xi'an Jiaotong University, Xi'an 710049, China*

## HIGHLIGHTS

- Different amounts of oxygen species and vacancies were constructed on $In_2O_3$.
- The *COOH pathway for $CO_2$ reduction to formate production on $In_2O_3$ was confirmed.
- 8.33% solar-to-formate and 10.11% solar-to-fuel were achieved when driven by photovoltaics.

## GRAPHICAL ABSTRACT
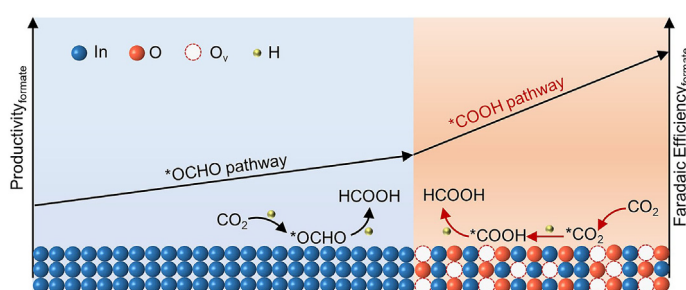


## ARTICLE INFO

## ABSTRACT

Indium-based oxides are promising electrocatalysts for producing formate via $CO_2$ reduction reaction, in which *OCHO is considered the key intermediate. Here, we identified that the *COOH pathway could be preferential to produce formate on $In_2O_3$ of $In/In_2O_3$ heterojunction due to the synergistic effect of oxygen species and vacancy. Specifically, *$CO_2$ and *COOH were observed on $In_2O_3$ and related to formate production by *in situ* Raman spectroscopy. The theoretical calculations further demonstrated that the energy barrier of the *COOH formation on $In_2O_3$ was decreased in the presence of oxygen vacancy, similar to or lower than that of the *OCHO formation on the In surface. As a result, a formate selectivity of over 90% was obtained on prepared $In/In_2O_3$ heterojunction with $343 \pm 7$ mA cm$^{-2}$ partial current density. Furthermore, when using a Si-based photovoltaic as an energy supplier, 10.11% solar–to–fuel energy efficiency was achieved.

## 1. Introduction

Converting $CO_2$ into fuels or chemical feedstocks is a promising strategy, which could alleviate the severity of the growing climate problem and recycle carbon resources [1–5]. The electrochemical $CO_2$ reduction reaction (ECO$_2$RR) proceeding at room temperature and pressure could utilize the electric energy generated from renewable energy like solar, wind, and tide, *etc.*, which has become an attractive approach for highly efficient production [6–8]. Among the reduction products such as methane [9,10], carbon monoxide (CO) [11], formate [12,13], ethanol [14,15], ethylene [16], and oxygenates involving more carbon (C$_{2+}$) [17,18], formate has some advantages. The low thermodynamic potential and overpotential of formate production enable higher energy conversion efficiency, which has greatly gained researchers' interest. Besides, formate as a liquid product is easier to transport back and forth compared to CO production, which also involves two electrons [19].

---

Recently, plenty of electrocatalysts have been explored to improve the activity and selectivity for $CO_2$ electroreduction and suppress the competing hydrogen evolution reduction (HER) [20,21]. Among them, $In_2O_3$, which is environmentally friendly and easy to be acquired, is one of the main electrocatalysts for formate production [22]. $In/In_2O_3$ heterojunction is the actual reacting electrocatalyst for the inevitable loss of O on $In_2O_3$ during the process of electrochemical $CO_2$ reaction [23]. To promote formate selectivity and activity on $In/In_2O_3$ heterojunction, great efforts have been devoted, such as size and morphology designing [24,25], defect engineering [26,27], single-atom design [28,29], doping introduction [22,30,31], and so on. However, only a few reports can achieve a current density over 300 mA cm$^{-2}$ with Faradaic efficiency of formate ($FE_{formate}$) above 90% [32].

On $In/In_2O_3$ heterojunction, it is proved that In is the main reaction site to produce formate because of the electronic-rich surface [30]. At this pathway, $CO_2$ is firstly dissolved in the electrolyte to form bicarbonate and absorbed on In surface for hydrogenation reaction. This causes a slow reaction rate for low $CO_2$ solubility [24]. However, as the ratio of oxygen species on the surface of $In/In_2O_3$ heterojunction increases, the pathway of formate production might be changed. $CO_2$ could be absorbed by hydroxyl group on $In_2O_3$ or In surface. This allows formate production at wider overpotential and higher productivity, which means that the number of oxygen species on the surface of $In/In_2O_3$ heterojunction could change the $CO_2$ adsorption mode [23]. In addition, oxygen vacancies ($O_v$) are also considered an effective method to improve formate formation on $In/In_2O_3$ by improving $CO_2$ activation [26,33].

Here, we constructed $In/In_2O_3$ heterojunctions with different amounts of oxygen species and $O_v$ to evaluate their electrochemical performance and explore the possible synergistic effect. *In situ* electrochemical surface-enhanced Raman spectroscopy (SERS) confirmed the *OCHO pathway for formate production on In sites of $In/In_2O_3$ heterojunction. Density-functional theory (DFT) calculations and SERS found that due to the synergistic effect of oxygen species and vacancy, the adsorption of *COOH was boosted and preferential to produce formate on $In_2O_3$ of $In/In_2O_3$ heterojunction. Subsequently, a Si-based photovoltaic and a gas diffusion electrode (GDE)-based electrolyzer were coupled using the optimized $In/In_2O_3$ heterojunction as a cathode.

## 2. Materials and methods

### 2.1. Synthesis of $In_2O_3$

The synthesis of prepared $In_2O_3$ is a typical hydrothermal method using a modified literature procedure (details in Supporting Information) [34]. First, $In(OH)_3$ was prepared using $InCl_3$ as indium resource. After vigorously stirring for 30 min, urea was added. The resulting solution was moved into a Teflon–lined stainless–steel autoclave and maintained at 120 °C for 12 h. A kind of white substance was collected. Then, $In_2O_3$ was obtained after calcinated at 500 °C for 2 h in different atmosphere.

### 2.2. Characterization

Surface morphology and element characterization were performed by field emission scanning electron microscope (FE–SEM), and energy dispersive X-ray spectroscopy (EDS). Lattice spacing and valence characterization were determined by X-ray diffraction (XRD), X-ray photoelectron spectroscopy (XPS), transmission electron microscope (TEM), and electron paramagnetic resonance (EPR).

### 2.3. Electrode fabrication

In electrode was sputtered onto carbon paper under the Ar atmosphere using magnetron sputtering apparatus. Bulk $In_2O_3$ was used directly without any further treatment. Before electrode fabrication, the catalyst ink, which was composed of the prepared sample, Nafion, and isopropanol, was ultrasonic for sufficient dispersion. Catalyst loading was measured by weighing carbon paper before and after spray coating repeatedly. Before testing, the GDE was put still at room temperature in air overnight.

The anode for the photovoltaic-electrolyzer (PV-EC) system was fabricated by carrying out electrodeposition on Ni foam reported before [35]. The electrolyte containing $Ni(NO_3)_3 \cdot 6H_2O$ and $Fe(NO_3)_3 \cdot 9H_2O$ was put in a breaker bathing in water to maintain 10 °C. The deposition was carried out on nickel foam at −1 V (vs Ag/AgCl) for 300 s.

### 2.4. Electrochemical performance measurements

The customized flow cell electrolyzer with three electrodes was used to conduct property tests on catalysts. The prepared GDE, leak-free Ag/AgCl, and platinum net acted as working electrode, reference electrode, and counter electrode, respectively. A piece of anion exchange membrane was put between catholyte chamber and anolyte chamber. An Auto-lab electrochemical workstation acted as energy supplier for all electrochemical measurements. Electrode potential was converted to reversible hydrogen electrode (RHE) considering the effect of pH and 80% *iR* compensation. The *iR* compensation was determined by electrochemical impedance spectroscopy measurement. During the process of $CO_2$RR experiments, 1 M KOH solution was consistently pumped into the anolyte and catholyte chamber. The flow rate of $CO_2$ was maintained feeding continually into GDE by a mass flowmeter controller. Linear sweep voltammetry (LSV) was conducted at a scanning rate of 10 mV s$^{-1}$. The electrochemical active surface area was obtained under $N_2$–purged 1 M KOH electrolyte. Electrochemical impendence spectroscopy was carried out from 100 KHz to 0.1 Hz.

### 2.5. In situ SERS measurements

The *in situ* SERS spectra were acquired using surface-enhanced Raman from Horiba, Lab RAM HR. The *in situ* Raman measurement was conducted using a customized electrocatalysis $CO_2$ reduction reactor, in which counter electrode was mounted far away from working electrode to avoid the effect of oxygen generating from counter electrode. To ensure the same condition, the three-electrodes system connected to an electrochemical workstation was just the same as the electrochemical performance test. Electrolyte was also pumped to chamber at the same flow rate by employing the same peristaltic tubing pump.

### 2.6. Computational method

The Vienna ab initio Simulation Package (VASP) was used to perform DFT calculations with plane-wave basis and periodic boundary conditions [36,37]. The Perdew–Burke–Ernzerhof (PBE) form of the generalized–gradient approximation (GGA) was chosen for electron exchange and correlation [38]. Three layers of In–O atoms were used for a small fluctuation within 0.1 eV and the fast-single electron step (Fig. S30). The lattice parameters of $In_2O_3(111)$ and In(101) were presented in Fig. S31. The stable configuration of $In_2O_3$–In was obtained by varying layer spacings. The solvation effects of aqueous electrolytes were considered by adding the solvation flag "LSOL=.TRUE., EB_k=78.4" (Table S4). The free energy change at the different potential was described by changing the applied potential in the CHE model (more details in Supporting Information) [39,40].

## 3. Results and discussion

### 3.1. Introduction of different amount of $O_v$ on $In_2O_3$

Flowerlike $In(OH)_3$ was chosen as the precursor for enhanced anti-reduction capacity (Supplementary information) [23,34]. Then, heat treatment was carried out at 500 °C in pure $O_2$ ($In_2O_3$–O) or air ($In_2O_3$–A) atmosphere (Fig. 1a). The phase transformation occurred slowly, and the
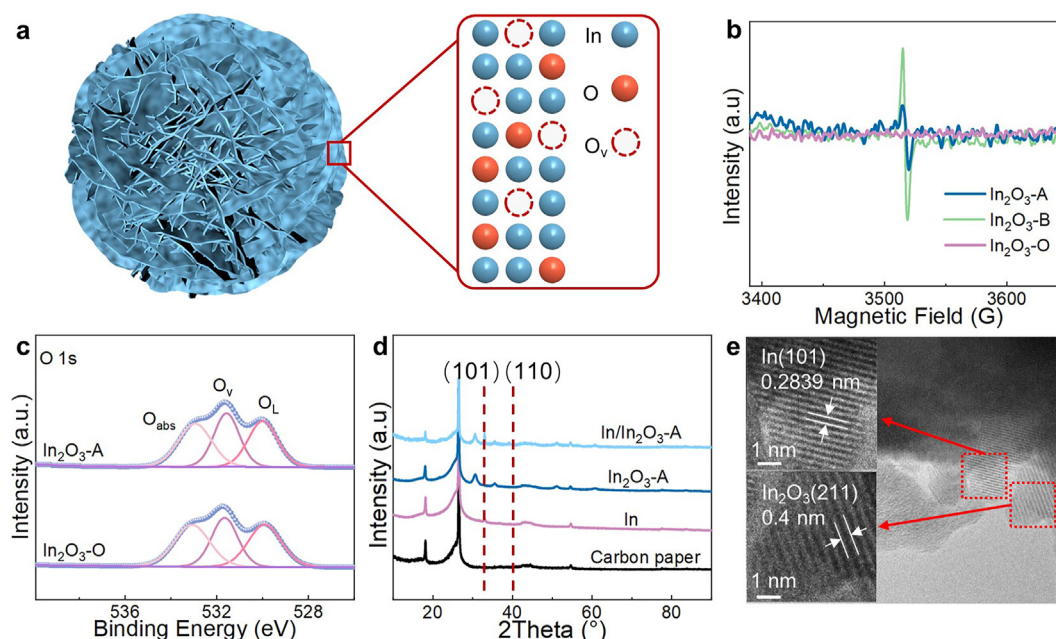
**Fig. 1.** Structural characterizations. (a) Schematic illustration of $In_2O_3$–A. (b) EPR of $In_2O_3$–A, $In_2O_3$–B, and $In_2O_3$–O. (c) O 1s XPS of $In_2O_3$–A and $In_2O_3$–B. (d) XRD of $In_2O_3$–A before and after *in situ* electroreduction. (e) TEM images of $In/In_2O_3$–A heterojunction.

white precursor $In(OH)_3$ would be converted to a faint yellow sample. As shown in Fig. S1, Raman peaks located at 130, 213, 309, 368, and 495 $cm^{-1}$ belong to the characteristics of $In_2O_3$. It is suggested that the prepared $In_2O_3$ is a cubic phase with three main peaks of (222), (400), and (440) (Fig. S2). Morphology structure and elemental mapping show that $In_2O_3$ remains a flowerlike structure of a 9 μm diameter with uniform distribution of In and O elements (Figs. S3−S5 and Table S1). This leads to a surface area of 3.5 times larger than bulk $In_2O_3$ ($In_2O_3$–B) (Fig. S6). The lattice spacing of 0.29 nm is corresponding to the $In_2O_3$ (222) (Fig. S7). Importantly, due to the $O_2$ atmosphere, no signal was detected for $In_2O_3$–O, as shown in Fig. 1b. In comparison, $In_2O_3$–A obtained in the air atmosphere has 50.29% $O_v$ which is higher than that of $In_2O_3$–O with 47.87% but a little less than $In_2O_3$–B with 50.41%, as shown in Figs. 1c and S8.

### 3.2. Enhanced formate production due to the abundant oxygen species and $O_v$

The electrochemical performance was evaluated using a self-made three-electrode flow cell (Fig. S9). The electrode was fabricated by spraying the ink containing catalysts and Nafion onto a carbon paper substrate, which was served as the working electrode. $In/In_2O_3$ heterojunction was subsequently constructed through *in situ* electroreduction, which was carried out using cyclic voltammetry (CV) for two cycles (Fig. S10). After that, the electrochemical active surface area suggests that $In/In_2O_3$–A heterojunction has a 1.7 mF $cm^{-2}$ electrochemical double electric layer capacitance, which is much higher than 0.7 mF $cm^{-2}$ of $In/In_2O_3$–B and 0.4 mF $cm^{-2}$ of In. This implies that more electrochemical active sites exist on $In/In_2O_3$–A heterojunction (Fig. S11 and Table S2). XRD displays that the two peaks at 32.9 and 36.7 of $In/In_2O_3$–A heterojunction are corresponding to In(101) and (110), respectively (Figs. 1d and S12). Figs. 1e, S13, and S14 suggest the existence of In and $In_2O_3$ on the surface of the $In/In_2O_3$–A. Lower electron transfer resistance for $In/In_2O_3$–A is also achieved (Fig. S15). As the potential becomes more negative, $In/In_2O_3$–A heterojunction exhibits a significantly faster increase in current density, indicating $In/In_2O_3$–A heterojunction possesses superior electrochemical activity, as shown in Fig. 2a. To investigate and measure the Faradaic efficiency (FE) of products under different potentials, the $ECO_2RR$ tests were carried out.

During the test, $In/In_2O_3$–A heterojunction showed an almost linear relationship between potential and time, indicating its better stability compared to the other catalyst (Fig. S16). Formate is the main product generated by all samples at relatively positive potentials, with few $H_2$ and CO produced, as shown in Figs. 2b and S17. When the potential turns more negative, $In/In_2O_3$–A heterojunction maintains high formate selectivity compared to $In/In_2O_3$–B, $In/In_2O_3$–O heterojunction and In, with a $FE_{formate}$ of 90.5% at −1.29 V. Meanwhile, $FE_{CO}$ and $FE_{H_2}$ are 2.12% and 8%, respectively. The maximum $FE_{formate}$ of $In/In_2O_3$–A heterojunction is found to be 94.9% at −1.02 V. Additionally, a formate partial current density of 343 ± 7 mA $cm^{-2}$ is obtained at −1.37 V, along with a formate yield of 6399 ± 131 μmol $cm^{-2}$ $h^{-1}$, exceeding most previously reported $In/In_2O_3$ heterojunctions (Figs. 2c, S18, and Table S7).

Few reports have carried out stability tests over 150 mA $cm^{-2}$ for the gradual loss of oxygen element of $In_2O_3$ during the process of electrolysis, resulting in severe hydrogen evolution reaction [23,24,32]. Here, an 8-h stability test at 200 mA $cm^{-2}$ of $In/In_2O_3$–A heterojunction is presented. The electrode potential exhibits only a slight change during the test, as shown in Figs. 2d and S19. The $FE_{formate}$ remains above 80% with a 160 mA $cm^{-2}$ partial current density and a constant product yield is observed, indicating a stable electrode composition and three-phase interfaces. These metrics suggest that $In/In_2O_3$–A heterojunction could be considered a promising electrocatalyst for its feasibility. Although a larger specific surface area may lead to higher current density, potential-dependent selectivity of formate demonstrates that specific surface area is not the main reason for improved selectivity at a wide potential range.

After *in situ* electroreduction by CV, a stable structure of $In_2O_3$ and In are constructed. The valence state of the indium element before and after the reaction is further verified. 444.5 eV and 452.1 eV are the reduced $In^0$ $3d_{5/2}$ and $3d_{3/2}$ after comparison with In electrode, as shown in Fig. 2e. The binding energy of $In^{3+}$ is considered higher than $In^0$ [23,41]. Therefore, 445.7 eV and 453.5 eV are corresponding to $In^{3+}$ $3d_{5/2}$ and $3d_{3/2}$, respectively. It suggests that the ratio of $In^{3+}$ on $In/In_2O_3$–A and $In/In_2O_3$–O heterojunction are 27.1% and 27.4%, respectively, higher than 5.2% of $In/In_2O_3$–B heterojunction (Fig. 2f). This demonstrates that more oxygen species are present on the surface of $In/In_2O_3$–A and $In/In_2O_3$–O heterojunction. In addition, clear flowerlike structure and
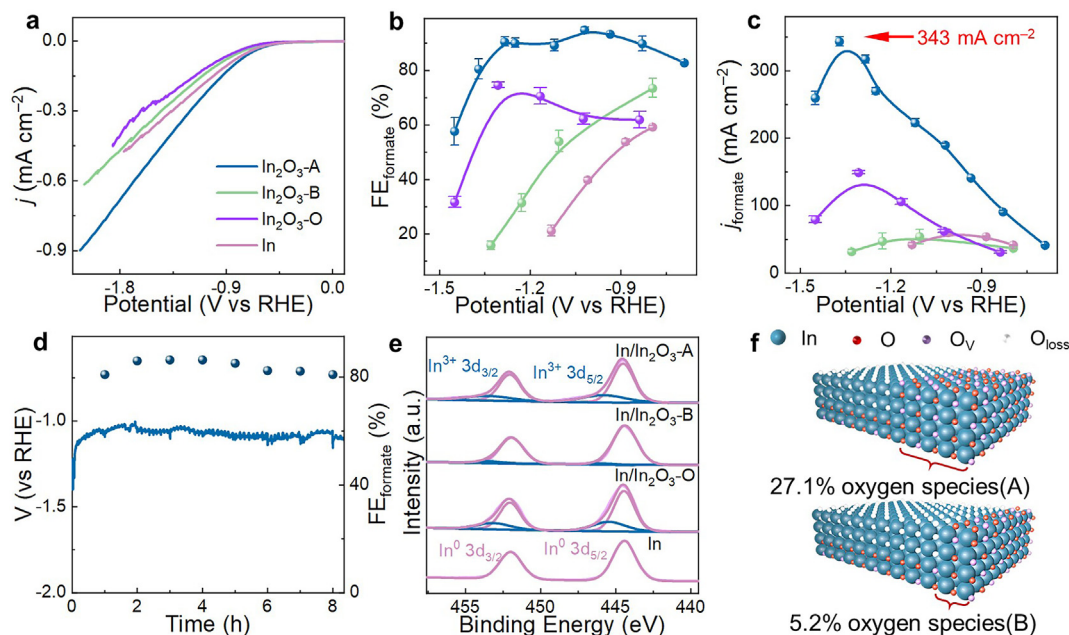
**Fig. 2.** Electrochemical $CO_2$ reduction performance of $In/In_2O_3$–A, $In/In_2O_3$–B, $In/In_2O_3$–O, and In. (a) LSV. (b) Potential-dependent $FE_{formate}$. (c) Partial current densities of formate. (d) Stability test at 200 mA cm$^{-2}$ of $In/In_2O_3$–A. (e) In 3d XPS of three types of $In/In_2O_3$ heterojunction and In after reaction at $-1.22$ V vs RHE. (f) Schematic illustration of oxygen species on the surface of $In/In_2O_3$–A and $In/In_2O_3$–B.

Raman characteristic peaks after reaction at different current densities also show that $In/In_2O_3$–A and $In/In_2O_3$–O heterojunction have stronger anti-reduced capacity (Fig. S20). Meanwhile, Although $In/In_2O_3$–B has more $O_v$, which has been proven to enhance $CO_2$ reduction performance by suppressing HER, it cannot achieve high formate selectivity at a wide range of potential without enough oxygen species [26]. $In/In_2O_3$–O has enough oxygen species and could maintain selectivity to formate at higher overpotential, while it prefers for HER on oxygen species without $O_v$, which explains lower electrochemical activity. Consequently, considering improving the performance of formate production of $In/In_2O_3$–A heterojunction with abundant oxygen species and $O_v$ (Fig. S21), we speculate that the $O_v$ protected by abundant oxygen species might be the key structure for highly formate production on $In/In_2O_3$–A heterojunction.

### 3.3. The detection of intermediates and possible reaction pathways for formate production

The insight for improving catalytic performance of $O_v$ protected by oxygen species was investigated. The *in situ* SERS test was implemented to identify possible intermediates of all samples in homemade Raman cell (Fig. S22). $In/In_2O_3$ heterojunction was constructed by CV. Each peak observed not caused by the changes in applied potential was analyzed first. Before immersing GDE into the electrolyte and applying potential, two main peaks were detected at 1350 cm$^{-1}$ and 1615 cm$^{-1}$, which were the Eg and Dg of carbon paper by comparing the GDE with and without catalyst, as shown in Fig. S23 [32]. After introducing 1 M KOH electrolyte, a huge peak appeared after 3000 cm$^{-1}$, attributed to adsorbed water on the surface of the catalyst. Another two new peaks were observed at 1065 cm$^{-1}$ and 1013 cm$^{-1}$, corresponding to the vibration of potassium carbonate when introducing $CO_2$ to the back of GDE [42]. Open circuit potential was then applied to the electrode, without any significant change for all three electrodes. Electrode potential was applied at the range of $-0.32$ V to $-1.52$ V vs RHE with the recording of signals. Between 900 cm$^{-1}$ and 1800 cm$^{-1}$, another three new peaks appeared at 1155 cm$^{-1}$, 1380 cm$^{-1}$, and 1530 cm$^{-1}$ on $In/In_2O_3$ heterojunction, as shown in Figs. 3a and b, and S24. Comparing the computed value (Fig. S25) and previously reported works [42–44], we concluded that the

first and last peaks were the unprotonated intermediates, which were the C=O stretching vibration of adsorbed carbonate ($v_s$ COO$^-$) and the C–O stretching vibration mode ($v_{as}$ COO$^-$), respectively [42,43,45,46]. The second peak was protonated intermediates, which was the C–O stretching of *COOH intermediate (Fig. 3c, in red dashed lines) [42,43,47]. As for $In/In_2O_3$–O with more oxygen species but less vacancy has weak signal of *COOH. $In/In_2O_3$–B with less oxygen species but more vacancy has a higher signal. Furthermore, $In/In_2O_3$–A exhibited the highest *COOH Raman signal for the more oxygen species and vacancy (Fig. 3c, the first arrow). Between 2700 cm$^{-1}$ and 3200 cm$^{-1}$, a new peak of the C–H bond in *OCHO on all electrodes was confirmed located at 2814 cm$^{-1}$ [42].

Next, the possible reaction pathways of enhanced formate production on $In/In_2O_3$–A heterojunction are further analyzed. It is clear that the reaction intermediate on In for $CO_2$ reduction to formate only involves *OCHO. $In/In_2O_3$–A and $In/In_2O_3$–O have same ratio of oxygen species and $In^0$ on the surface and nearly the same intensity of *OCHO, as shown in Fig. S26. Meanwhile, $In/In_2O_3$–B has higher ratio of $In^0$ and higher intensity of *OCHO, which implies that *OCHO might only exist on $In^0$. *$CO_2$ and *COOH just existed on the $In_2O_3$ surface of $In/In_2O_3$. *$CO_2$ was rich on the surface of $In/In_2O_3$–A due to the abundant oxygen species and $O_v$ (Figs. S27 and S28). Furthermore, the Raman signal of *COOH on $In/In_2O_3$–A was higher than that on $In/In_2O_3$–B and $In/In_2O_3$–O (Fig. 3c). It means that the $CO_2$-rich environment on $In/In_2O_3$–A influenced the reaction pathway involving *COOH. Some reports think that *COOH is the reaction intermediate to produce CO, while HER rather than CO production is the main competing reaction here (Fig. S29) [48,49]. Therefore, the *$CO_2$ and *COOH might be the reaction intermediates for formate production, which has been reported on Sn-based electrocatalysts [33,47,50–52].

### 3.4. The energy barrier analysis of the possible reaction pathway for formate production

To verify the assumed reacting pathways, DFT was used to analyze the energy barrier of the possible reaction pathway. On the $In_2O_3$ surface, we found two types of *$CO_2$ configurations, with the C–O bond parallel to the surface or V-shaped symmetric adsorption. The hydrogenation of
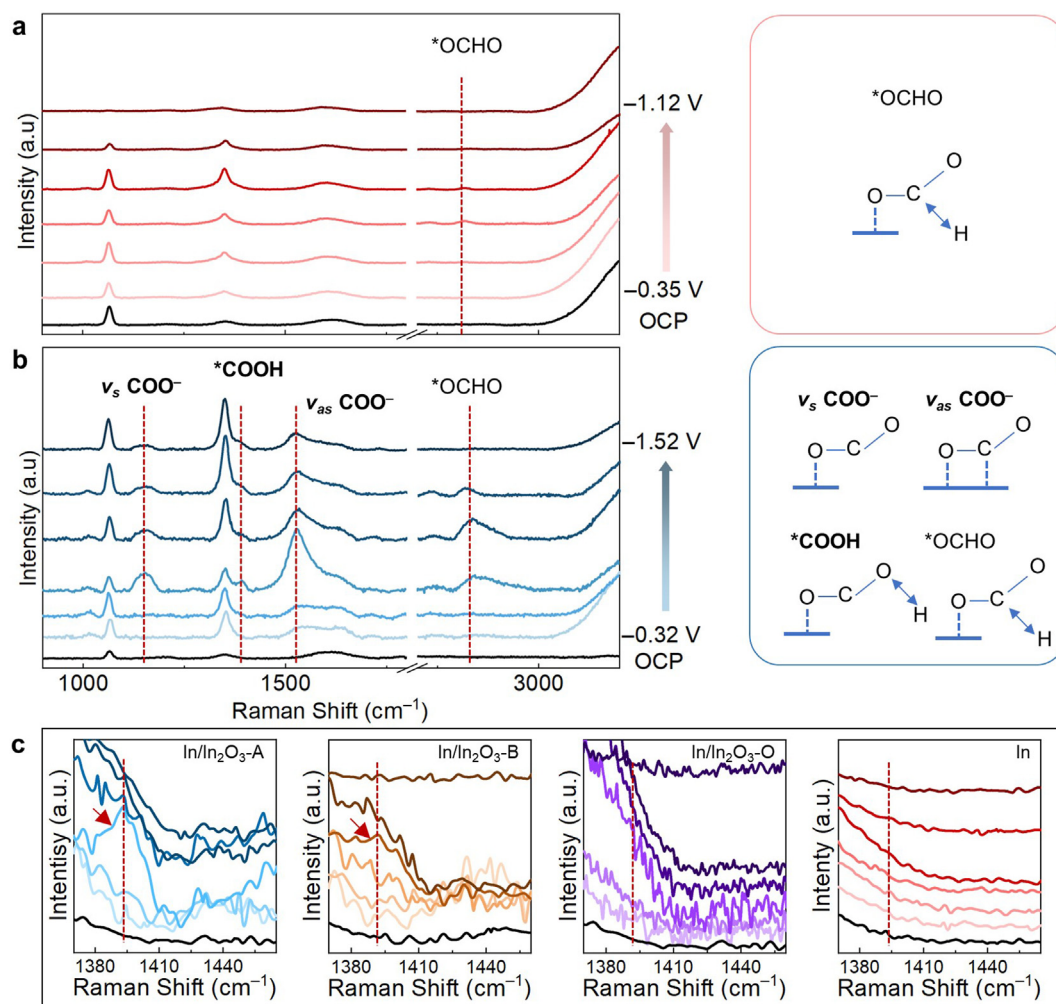
**Fig. 3.** The potential-dependent *in situ* SERS spectra. (a) In. (b) In/In$_2$O$_3$–A between 900–1800 cm$^{-1}$ and 2700–3200 cm$^{-1}$. *OCHO was observed on both catalysts, while $v_s$ COO$^-$, $v_{as}$ COO$^-$, and *COOH were only observed on In/In$_2$O$_3$ heterojunction. (c) *In situ* Raman signal of *COOH at three types of In/In$_2$O$_3$ and In.

*CO$_2$ to form *COOH or *OCHO intermediates can be achieved by adding H$^+$ to O or C atoms. The influence of two types of *CO$_2$ named 1 and 2 on the reaction pathway was analyzed by removing the surface O that bonds with *CO$_2$ (Fig. S32).

*CO$_2$ adsorption is present and related to crystal facets as well as catalysts during the reaction process [47,53]. DFT results show CO$_2$ cannot form a stable bond with In surface, consistent with Raman signal. On the surface of In$_2$O$_3$, *HCOOH is easier for direct desorption. On the In surface (Fig. 4a), as the *OCHO has lower Gibbs free energy than *COOH, formate produced from the *OCHO pathway is preferred, with an energy barrier of 0.656 eV, lower than 0.919 eV via the *COOH pathway. The presence of surface O on In$_2$O$_3$ can facilitate the adsorption of CO$_2$ and *COOH intermediates compared to In. However, the stronger adsorption of *COOH makes desorption more challenging (Fig. S33 and Table S3). After the introduction of O$_v$ (In$_2$O$_3$–O$_v$), although the *OCHO is the minimum energy pathway and more stable than *COOH, its desorption is hard, leading to surface accumulation and poisoning of active sites (consistent with the gradual enhancement phenomenon of *OCHO intensity on *in situ* Raman spectroscopy in Fig. S26b). When considering the limiting potential at which each step is thermodynamically favorable, the limiting potential for the *COOH pathway is similar to (0.646 eV) or even lower (0.478 eV) than the *OCHO pathway for formate production on the In surface. These variations suggest that the electroreduction of CO$_2$ to formate through the *COOH pathway on the In$_2$O$_3$–O$_v$ surface is also allowed. When applying the corresponding

potential to the electrode, such as −0.656 V, −1.009 V, and −1.41 V vs RHE (based on Table S3), the pathway in which every step is exothermic will open, following the order about the lowest limiting potential. For example, at −0.656 V vs RHE, the *COOH pathway is thermodynamically favorable in In$_2$O$_3$-2-O$_v$ while the *OCHO pathway is blocked due to the higher desorption barrier (Fig. S34). At −1.009 V vs RHE, *COOH and *OCHO pathways are both favorable in In$_2$O$_3$-2-O$_v$ and In surface (Fig. S35). At −1.41 V vs RHE, *COOH and *OCHO pathways are both thermodynamically favorable in In$_2$O$_3$-1-O$_v$ and In$_2$O$_3$-2-O$_v$ surface (Fig. S36). More details are discussed in Supplementary information.

The reason for the enhanced adsorption capacity of *COOH compared to the In was explored by Crystal orbital Hamilton population (COHP) analysis and Bader charge [54–56]. Due to the existence of oxygen species, In atom has a higher positive charge on the In$_2$O$_3$ surface than on the pure In, with the Bader charge increased from 0.32 to 1.76, as shown in Figs. 4b and c, and S37. The more electropositive In will have a stronger binding ability to the O atom in *COOH. On both In$_2$O$_3$–O$_v$ and In surfaces, the integrated COHP (−ICOHP) of the C–In bond remains around 3.4, indicating similar C–In bond adsorption strength. However, the −ICOHP of the C–O bond increases from 1.58 on the In surface to 3.26 on the In$_2$O$_3$–O$_v$ surface. The above results indicate that the enhanced adsorption capacity of *COOH on the In$_2$O$_3$-O$_v$ surface mainly comes from its stronger O–In bond interaction. In conclusion, the *COOH pathway on In$_2$O$_3$–O$_v$, as well as the *OCHO pathway on In/In$_2$O$_3$-Ov, explains the more efficient formate production on In/In$_2$O$_3$–A (Fig. 4d).
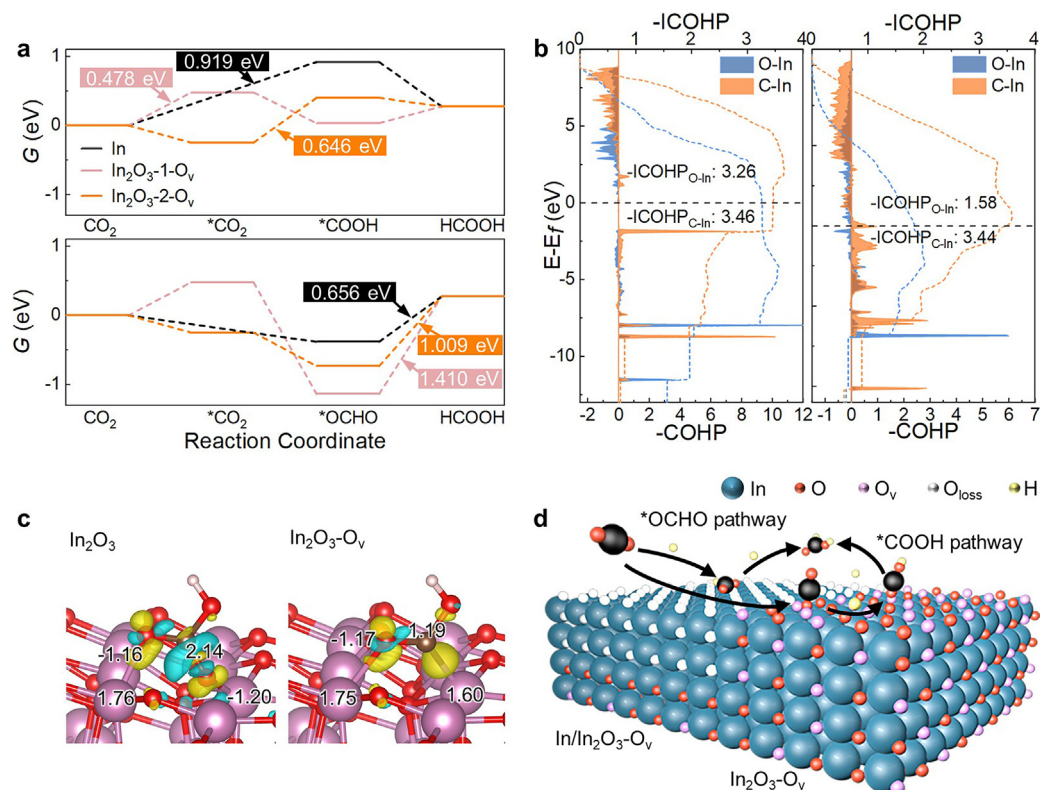
**Fig. 4.** The evaluation of possible reaction pathway. (a) Gibbs free-energy diagrams of $CO_2$ reduction to formate on In and $In_2O_3$–$O_v$ through *COOH (upper panel) and *OCHO (lower panel) pathways, respectively at 0 V vs RHE. (b) The –ICOHP analysis of C–O bond and C–In bond on $In_2O_3$–$O_v$ and In surfaces. (c) The results of calculated charge density among In and O atoms. (d) Schematic illustration of two types of reaction pathways on $In_2O_3$–$O_v$ and $In/In_2O_3$–$O_v$ surfaces, respectively.
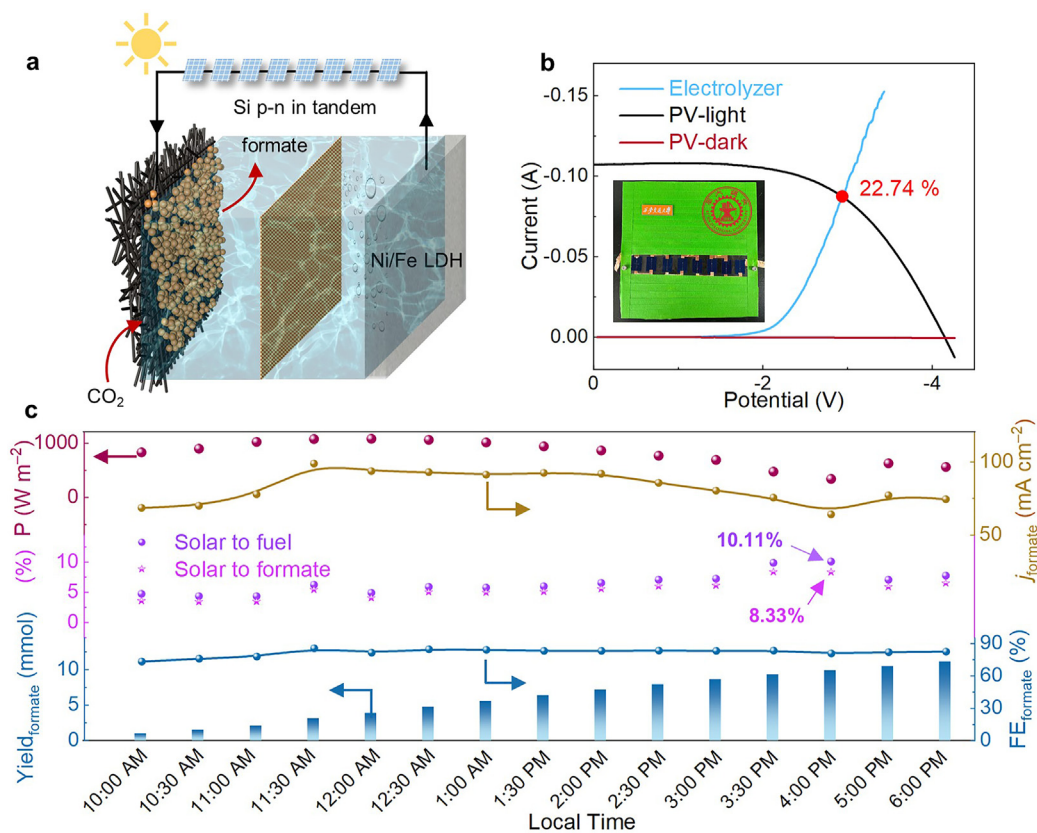


**Fig. 5.** The results of the solar-driven formate production. (a) Schematic illustration of PV-driven $CO_2RR$ system. (b) The current–potential (j–$V_{cell}$) curve of Si-based solar cells at 476 W m$^{-2}$ illuminations and $CO_2RR$ electrolyzer. (c) Radiation intensity, photocurrent and partial current density of formate, solar to fuels and formate, FE$_{formate}$, and yield of formate distribution under natural light conditions.

## 3.5. Solar-driven formate production

The feasibility of formate production driven by sustainable energy was conducted by coupling the GDE-based $CO_2RR$ electrolyzer with a Si-based solar cell to power $CO_2$ reduction using solar energy (Figs. 5a and S38). In this system, the prepared $In/In_2O_3$–A heterojunction served as the cathode. The Ni/Fe LDH was successfully prepared and used as the anode due to lower overpotential than Pt (Figs. S39–S41) [35]. The electrolyzer was assembled as tested above. Eight commercial Si solar cell in tandem with 24.8 $cm^{-2}$ total illumination areas was used as an electric supplier. The PV cell was fixed on an auto-tracking model to make sure that the sunlight irradiated vertically onto the PV cell at all times [57]. As shown in Fig. 5c, after one natural day of 8 h, we got a maximum of 10.11% solar-to-fuel and 8.33% solar-to-formate energy conversion efficiency, exceeding most reported Si-based PV-EC (Table S5). Meanwhile, selectivity of formate remains over 88% with a maximum partial current density of 98 mA $cm^{-2}$. The productivity of formate grows smoothly to 11.15 mmol one day (Table S6). The best energy efficiency appears at 4:00 pm for the appropriate couple with 22.74% efficiency for the PV (Figs. 5b and S42).

## 4. Conclusions

In summary, we first prepared three types of $In/In_2O_3$ heterojunction with different amount of oxygen species and $O_v$. After electrochemical tests, $In/In_2O_3$ heterojunction containing more oxygen species as well as $O_v$ had higher formate production activity than that with only one feature. This indicated the synergistic effect between the oxygen species and $O_v$. The *in situ* SERS confirmed two types of unprotonated $*CO_2$ and $*COOH$ on the $In_2O_3$–$O_v$ surface, while the protonated $*OCHO$ existed on In surface. DFT calculation results showed that $CO_2$ could not form a stable bond with In atom, consistent with *in situ* SERS. Although $*CO_2$ could be achieved on $In_2O_3$ surface, the formate production was inhibited for the high$*COOH$ formation energy. Introduced $O_v$ greatly decreased the energy barrier of $*COOH$ formation on the $In_2O_3$ surface, which was similar to or lower than that of the $*OCHO$ pathway on In surface. In comparison, formate production via $*OCHO$ on the $In_2O_3$–$O_v$ surface was blocked for the higher energy barrier than $*COOH$. This leads to formate production via the $*COOH$ pathway on the $In_2O_3$–$O_v$ surface, as well as the $*OCHO$ pathway on the In surface. Furthermore, the prepared $In/In_2O_3$ heterojunction exhibits a formate selectivity over 80% under a wide potential range of $-0.69$ to $-1.37$ V vs RHE. Particularly, a formate partial current density of $343 \pm 7$ mA $cm^{-2}$ was achieved, exceeding previously reported $In/In_2O_3$ heterojunction. Under this fundamental understanding, a Si-based photovoltaic and GDE-based electrolyzer were coupled using the prepared $In/In_2O_3$ heterojunction as the cathode. Under natural light irradiation, 10.11% solar-to-fuel and 8.33% solar-to-formate energy efficiency were achieved, surpassing most reported Si-based PV-EC. This work provides a new strategy for collaborative utilization of oxygen species and $O_v$ to modulate the reaction pathway and enhance electrocatalytic $CO_2$ reduction for formate production and practical applications driven by sustainable energy.

## Author contributions

**Tengfei Ma:** Writing – original draft, Formal analysis, Data curation, Conceptualization. **Zihao Jiao:** Formal analysis, Conceptualization. **Haoran Qiu:** Methodology, Data curation. **Feng Wang:** Methodology, Formal analysis. **Ya Liu:** Writing – review & editing, Supervision, Formal analysis, Conceptualization. **Liejin Guo:** Writing – review & editing, Resources, Project administration, Conceptualization.

## Declaration of competing interest

The authors declare that they have no known competing financial interests or personal relationships that could have appeared to influence the work reported in this paper.

## Appendix A. Supplementary data

Supplementary data to this article can be found online at https://doi.org/10.1016/j.esci.2024.100246.

## References

[1] L. Li, X. Li, Y. Sun, Y. Xie, Rational design of electrocatalytic carbon dioxide reduction for a zero-carbon network, Chem. Soc. Rev. 51 (2022) 1234–1252.

[2] M.G. Kibria, J.P. Edwards, C.M. Gabardo, C.-T. Dinh, A. Seifitokaldani, D. Sinton, E.H. Sargent, Electrochemical $CO_2$ reduction into chemical feedstocks: from mechanistic electrocatalysis models to system design, Adv. Mater. 31 (2019) 1807166.

[3] M. Aresta, A. Dibenedetto, A. Angelini, Catalysis for the valorization of exhaust carbon: from $CO_2$ to chemicals, materials, and fuels. technological use of $CO_2$, Chem. Rev. 114 (2014) 1709–1742.

[4] S.J. Davis, N.S. Lewis, M. Shaner, S. Aggarwal, D. Arent, I.L. Azevedo, S.M. Benson, T. Bradley, J. Brouwer, Y.M. Chiang, C.T.M. Clack, A. Cohen, S. Doig, J. Edmonds, P. Fennell, C.B. Field, B. Hannegan, B.M. Hodge, M.I. Hoffert, E. Ingersoll, P. Jaramillo, K.S. Lackner, K.J. Mach, M. Mastrandrea, J. Ogden, P.F. Peterson, D.L. Sanchez, D. Sperling, J. Stagner, J.E. Trancik, C.J. Yang, K. Caldeira, Net-zero emissions energy systems, Science 360 (2018) eaas9793.

[5] Y. Liu, F. Wang, Z. Jiao, S. Bai, H. Qiu, L. Guo, Photochemical systems for solar-to-fuel production, Electrochem. Energy Rev. 5 (2022) 5.

[6] T.N. Nguyen, C.T. Dinh, Gas diffusion electrode design for electrochemical carbon dioxide reduction, Chem. Soc. Rev. 49 (2020) 7488–7504.

[7] D. Wang, J. Mao, C. Zhang, J. Zhang, J. Li, Y. Zhang, Y. Zhu, Modulating microenvironments to enhance $CO_2$ electroreduction performance, eScience 3 (2023) 100119.

[8] M. Wang, J. Luo, A coupled electrochemical system for $CO_2$ capture, conversion and product purification, eScience 3 (2023) 100155.

[9] Y. Li, A. Xu, Y. Lum, X. Wang, S.F. Hung, B. Chen, Z. Wang, Y. Xu, F. Li, J. Abed, J.E. Huang, A.S. Rasouli, J. Wicks, L.K. Sagar, T. Peng, A.H. Ip, D. Sinton, H. Jiang, C. Li, E.H. Sargent, Promoting $CO_2$ methanation via ligand-stabilized metal oxide clusters as hydrogen-donating motifs, Nat. Commun. 11 (2020) 6190.

[10] S. Bai, W. Jing, G. He, C. Liao, F. Wang, Y. Liu, L. Guo, Near-infrared-responsive photocatalytic $CO_2$ conversion via in situ generated $Co_3O_4/Cu_2O$, ACS Nano 17 (2023) 10976–10986.

[11] Y. Guo, H. Yang, X. Zhou, K. Liu, C. Zhang, Z. Zhou, C. Wang, W. Lin, Electrocatalytic reduction of $CO_2$ to CO with 100% faradaic efficiency by using pyrolyzed zeolitic imidazolate frameworks supported on carbon nanotube networks, J. Mater. Chem. A 5 (2017) 24867–24873.

[12] S. Yan, C. Peng, C. Yang, Y. Chen, J. Zhang, A. Guan, X. Lv, H. Wang, Z. Wang, T.K. Sham, Q. Han, G. Zheng, Electron localization and lattice strain induced by surface lithium doping enable ampere-level electrosynthesis of formate from $CO_2$, Angew. Chem. Int. Ed. 133 (2021) 25945–25949.

[13] T. Shi, D. Liu, N. Liu, Y. Zhang, H. Feng, Q. Li, Triple-phase interface engineered hierarchical porous electrode for $CO_2$ electroreduction to formate, Adv. Sci. 9 (2022) 2204472.

[14] L.R.L. Ting, O. Piqué, S.Y. Lim, M. Tanhaei, F. Calle-Vallejo, B.S. Yeo, Enhancing $CO_2$ electroreduction to ethanol on copper–silver composites by opening an alternative catalytic pathway, ACS Catal. 10 (2020) 4059–4069.

[15] Y. Liu, F. Yu, F. Wang, S. Bai, G. He, Construction of z-scheme $In_2S_3$-$TiO_2$ for $CO_2$ reduction under concentrated natural sunlight, Chin. J. Struc. Chem. 41 (2022) 2201034–2201039.

[16] C.T. Dinh, T. Burdyny, M.G. Kibria, A. Seifitokaldani, C.M. Gabardo, F.P. Garcia de Arquer, A. Kiani, J.P. Edwards, P. De Luna, O.S. Bushuyev, C. Zou, R. Quintero-Bermudez, Y. Pang, D. Sinton, E.H. Sargent, $CO_2$ electroreduction to ethylene via hydroxide-mediated copper catalysis at an abrupt interface, Science 360 (2018) 783–787.

[17] C.M. Gabardo, C.P. O'Brien, J.P. Edwards, C. McCallum, Y. Xu, C.-T. Dinh, J. Li, E.H. Sargent, D. Sinton, Continuous carbon dioxide electroreduction to concentrated multi-carbon products using a membrane electrode assembly, Joule 3 (2019) 2777–2791.

[18] S. Bai, H. Qiu, M. Song, G. He, F. Wang, Y. Liu, L. Guo, Porous fixed-bed photoreactor for boosting C–C coupling in photocatalytic $CO_2$ reduction, eScience 2 (2022) 428–437.

[19] J. Li, M. Zhu, Y.F. Han, Recent advances in electrochemical $CO_2$ reduction on indium-based catalysts, ChemCatChem 13 (2020) 514–531.

[20] Y. Liu, H. Qiu, J. Li, L. Guo, J.W. Ager, Tandem electrocatalytic $CO_2$ reduction with efficient intermediate conversion over pyramid-textured Cu-Ag catalysts, ACS Appl. Mater. Interfaces 13 (2021) 40513–40521.

[21] M. Song, Z. Jiao, W. Jing, Y. Liu, L. Guo, Revealing the nature of C-C coupling sites on a cu surface for $CO_2$ reduction, J. Phys. Chem. Lett. 13 (2022) 4434–4440.

[22] Y. Liang, W. Zhou, Y. Shi, C. Liu, B. Zhang, Unveiling *in situ* evolved In/In$_2$O$_{3-x}$ heterostructure as the active phase of In$_2$O$_3$ toward efficient electroreduction of $CO_2$ to formate, Sci. Bull. 65 (2020) 1547–1554.

[23] B. Wulan, X. Cao, D. Tan, J. Ma, J. Zhang, To stabilize oxygen on In/In$_2$O$_3$ heterostructure for efficient electrocatalytic $CO_2$ reduction, Adv. Funct. Mater. 23 (2022) 2209114.

[24] Y. Huang, X. Mao, G. Yuan, D. Zhang, B. Pan, J. Deng, Y. Shi, N. Han, C. Li, L. Zhang, L. Wang, L. He, Y. Li, Y. Li, Size-dependent selectivity of electrochemical $CO_2$ reduction on converted In$_2$O$_3$ nanocrystals, Angew. Chem. Int. Ed. 60 (2021) 15844–15848.

[25] Z. Wang, Y. Zhou, D. Liu, R. Qi, C. Xia, M. Li, B. You, B.Y. Xia, Carbon-confined indium oxides for efficient carbon dioxide reduction in a solid-state electrolyte flow cell, Angew. Chem. Int. Ed. 61 (2022) 202200552.

[26] Q. Cheng, M. Huang, L. Xiao, S. Mou, X. Zhao, Y. Xie, G. Jiang, X. Jiang, F. Dong, Unraveling the influence of oxygen vacancy concentration on electrocatalytic $CO_2$ reduction to formate over indium oxide catalysts, ACS Catal. 13 (2023) 4021–4029.

[27] J. Zhang, R. Yin, Q. Shao, T. Zhu, X. Huang, Oxygen vacancies in amorphous InO$_x$ nanoribbons enhance $CO_2$ adsorption and activation for $CO_2$ electroreduction, Angew. Chem. Int. Ed. 58 (2019) 5609–5613.

[28] P. Lu, X. Tan, H. Zhao, Q. Xiang, K. Liu, X. Zhao, X. Yin, X. Li, X. Hai, S. Xi, A.T.S. Wee, S.J. Pennycook, X. Yu, M. Yuan, J. Wu, G. Zhang, S.C. Smith, Z. Yin, Atomically dispersed indium sites for selective $CO_2$ electroreduction to formic acid, ACS Nano 15 (2021) 5671–5678.

[29] I. Grigioni, L.K. Sagar, Y.C. Li, G. Lee, Y. Yan, K. Bertens, R.K. Miao, X. Wang, J. Abed, D.H. Won, F.P. García de Arquer, A.H. Ip, D. Sinton, E.H. Sargent, $CO_2$ electroreduction to formate at a partial current density of 930 mA cm$^{-2}$ with InP colloidal quantum dot derived catalysts, ACS Energy Lett. 6 (2020) 79–84.

[30] B. Pan, G. Yuan, X. Zhao, N. Han, Y. Huang, K. Feng, C. Cheng, J. Zhong, L. Zhang, Y. Wang, Y. Li, Highly dispersed indium oxide nanoparticles supported on carbon nanorods enabling efficient electrochemical $CO_2$ reduction, Small Sci. 1 (2021) 2100029.

[31] T. Shi, D. Liu, H. Feng, Y. Zhang, Q. Li, Evolution of triple-phase interface for enhanced electrochemical $CO_2$ reduction, Chem. Eng. J. 431 (2022) 134348.

[32] Z. Liu, X. Lv, J. Zhang, A. Guan, C. Yang, S. Yan, Y. Chen, K. Liu, G. Zheng, Hydroxy–group–enriched In$_2$O$_3$ facilitates $CO_2$ electroreduction to formate at large current densities, Adv. Mater. Interfaces 9 (2022) 2101956.

[33] Z. Li, A. Cao, Q. Zheng, Y. Fu, T. Wang, K.T. Arul, J.L. Chen, B. Yang, N.M. Adli, L. Lei, C.L. Dong, J. Xiao, G. Wu, Y. Hou, Elucidation of the synergistic effect of dopants and vacancies on promoted selectivity for $CO_2$ electroreduction to formate, Adv. Mater. 33 (2021) 2005113.

[34] H. Zhu, X. Wang, Z. Wang, C. Yang, F. Yang, X. Yang, Self-assembled 3D microflowery In(OH)$_3$ architecture and its conversion to In$_2$O$_3$, J. Phys. Chem. C 112 (2008) 15285–15292.

[35] X. Lu, C. Zhao, Electrodeposition of hierarchically structured three-dimensional nickel-iron electrodes for efficient oxygen evolution at high current densities, Nat. Commun. 6 (2015) 6616.

[36] G. Kresse, J. Furthmüller, Efficient iterative schemes for ab initio total-energy calculations using a plane-wave basis set, Phys. Rev. B 54 (1996) 11169–11186.

[37] G. Kresse, J. Furthmüller, Efficiency of ab-initio total energy calculations for metals and semiconductors using a plane-wave basis set, Comput. Mater. Sci. 6 (1996) 15–50.

[38] J.P. Perdew, K. Burke, M. Ernzerhof, Generalized gradient approximation made simple, Phys. Rev. Lett. 77 (1996) 3865–3868.

[39] S. Wang, V. Petzold, V. Tripkovic, J. Kleis, J.G. Howalt, E. Skúlason, E.M. Fernández, B. Hvolbæk, G. Jones, A. Toftelund, H. Falsig, M. Björketun, F. Studt, F. Abild-Pedersen, J. Rossmeisl, J.K. Nørskov, T. Bligaard, Universal transition state scaling relations for (de)hydrogenation over transition metals, Phys. Chem. Chem. Phys. 13 (2011) 20760–20765.

[40] S. Wang, B. Temel, J. Shen, G. Jones, L.C. Grabow, F. Studt, T. Bligaard, F. Abild-Pedersen, C.H. Christensen, J.K. Nørskov, Universal Brønsted-Evans-Polanyi relations for C–C, C–O, C–N, N–O, N–N, and O–O dissociation reactions, Catal. Lett. 141 (2011) 370–373.

[41] W. Yang, Y. Zhao, S. Chen, W. Ren, X. Chen, C. Jia, Z. Su, Y. Wang, C. Zhao, Defective indium/indium oxide heterostructures for highly selective carbon dioxide electrocatalysis, Inorg. Chem. 59 (2020) 12437–12444.

[42] Z. Pan, K. Wang, K. Ye, Y. Wang, H.-Y. Su, B. Hu, J. Xiao, T. Yu, Y. Wang, S. Song, Intermediate adsorption states switch to selectively catalyze electrochemical $CO_2$ reduction, ACS Catal. 10 (2020) 3871–3880.

[43] J. Duan, T. Liu, Y. Zhao, R. Yang, Y. Zhao, W. Wang, Y. Liu, H. Li, Y. Li, T. Zhai, Active and conductive layer stacked superlattices for highly selective $CO_2$ electroreduction, Nat. Commun. 13 (2022) 2039.

[44] S. Wang, Z. Wu, C. Xu, S. Jiang, H.Q. Peng, W. Zhang, B. Liu, Y.F. Song, Triple-phase interface engineering over an In$_2$O$_3$ electrode to boost carbon dioxide electroreduction, ACS Appl. Mater. Interfaces 14 (2022) 45423–45432.

[45] W. Wang, X. Wang, Z. Ma, Y. Wang, Z. Yang, J. Zhu, L. Lv, H. Ning, N. Tsubaki, M. Wu, Carburized In$_2$O$_3$ nanorods endow $CO_2$ electroreduction to formate at 1 A cm$^{-2}$, ACS Catal. 13 (2022) 796–802.

[46] W. Shan, R. Liu, H. Zhao, Z. He, Y. Lai, S. Li, G. He, J. Liu, In situ surface-enhanced Raman spectroscopic evidence on the origin of selectivity in $CO_2$ electrocatalytic reduction, ACS Nano 14 (2020) 11363–11372.

[47] T. Tsujiguchi, Y. Kawabe, S. Jeong, T. Ohto, S. Kukunuri, H. Kuramochi, Y. Takahashi, T. Nishiuchi, H. Masuda, M. Wakisaka, K. Hu, G. Elumalai, J.-i. Fujita, Y. Ito, Acceleration of electrochemical $CO_2$ reduction to formate at the Sn/reduced graphene oxide interface, ACS Catal. 11 (2021) 3310–3318.

[48] B.-H. Zhao, F. Chen, M. Wang, C. Cheng, Y. Wu, C. Liu, Y. Yu, B. Zhang, Economically viable electrocatalytic ethylene production with high yield and selectivity, Nat. Sustain. 6 (2023) 827–837.

[49] X. Zhi, Y. Jiao, Y. Zheng, A. Vasileff, S.-Z. Qiao, Selectivity roadmap for electrochemical $CO_2$ reduction on copper-based alloy catalysts, Nano Energy 71 (2020) 104601.

[50] Y. Zang, T. Liu, H. Li, P. Wei, Y. Song, C. Cheng, D. Gao, Y. Song, G. Wang, X. Bao, In situ reconstruction of defect-rich SnO$_2$ through an analogous disproportionation process for $CO_2$ electroreduction, Chem. Eng. J. 446 (2022) 137444.

[51] Y. Ito, S. Kukunuri, S. Jeong, G. Elumalai, A.A. Haji Tajuddin, Z. Xi, K. Hu, T. Ohto, Phase-dependent electrochemical $CO_2$ reduction ability of NiSn alloys for formate generation, ACS Appl. Energy Mater. 4 (2021) 7122–7128.

[52] S. Jeong, T. Ohto, T. Nishiuchi, Y. Nagata, J.-i. Fujita, Y. Ito, Polyethylene glycol covered Sn catalysts accelerate the formation rate of formate by carbon dioxide reduction, ACS Catal. 11 (2021) 9962–9969.

[53] J. Ko, B.-K. Kim, J.W. Han, Density functional theory study for catalytic activation and dissociation of $CO_2$ on bimetallic alloy surfaces, J. Phys. Chem. C 120 (2016) 3438–3447.

[54] R. Dronskowski, P.E. Bloechl, Crystal orbital Hamilton populations (COHP): energy-resolved visualization of chemical bonding in solids based on density-functional calculations, J. Phys. Chem. C 97 (1993) 8617–8624.

[55] V.L. Deringer, A.L. Tchougréeff, R. Dronskowski, Crystal orbital Hamilton population (COHP) analysis as projected from plane-wave basis sets, J. Phys. Chem. A 115 (2011) 5461–5466.

[56] S. Maintz, V.L. Deringer, A.L. Tchougréeff, R. Dronskowski, LOBSTER: a tool to extract chemical bonding from plane-wave based DFT, J. Comput. Chem. 37 (2016) 1030–1035.

[57] S. Bai, M. Song, T. Ma, F. Wang, Y. Liu, L. Guo, On factors of ions in seawater for $CO_2$ reduction, Appl. Catal. B 323 (2023) 122166.